Electronic Supplementary Information

Phase diagram of conformationally asymmetric pentablock copolymer melts: a theory and simulation study

Tristan Myers,[§a] So Jung Park,[§a] Arthi Jayaraman*[a,b,c]

a. Department of Chemical and Biomolecular Engineering, University of Delaware, Colburn Lab, 150 Academy Street, Newark, DE 19716

b. Department of Materials Science and Engineering, University of Delaware, DuPont Hall, 127 The Green, Newark, DE 19716

c. Data Science Institute, University of Delaware, Newark, DE 19716

*** Corresponding author**: arthij@udel.edu

[§] T.M. and S.J.P. contributed equally to the article

Table S1 *The structure details and spatial discretization for the candidate phases in the SCFT calculations. The table lists body-centered cubic sphere (BCC), hexagonally-packed cylinders (C_6), double gyroid (DG), Fddd orthorhombic network (O^{70}), and lamellae (L) morphologies. The initial guess field for SCFT calculation for each candidate morphology is easily accessible by the level set or form factor methods.*[1]

Name	Structure	Space group	Crystal System	SCFT Grid Size
BCC	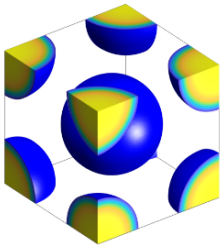	$Im\bar{3}m$	Cubic	$64 \times 64 \times 64$
C_6	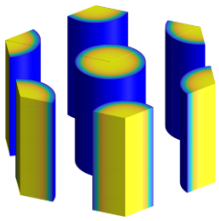	$p6mm$		64×64
DG	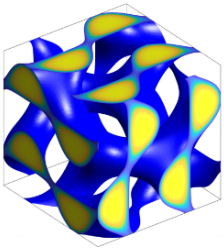	$Ia\bar{3}d$	Cubic	$64 \times 64 \times 64$
O^{70}	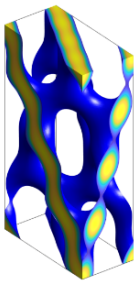	$Fddd$	Orthorhombic	$32 \times 64 \times 128$
L	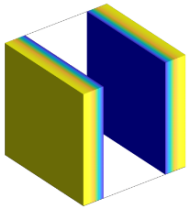			128

Table S2 *Homopolymer chain designs for calibration simulations and β/β_{ref} sampled from each melt, where $\beta = \sqrt{R_g^2/V_{chain}}$. Homopolymer designs are given in terms of the number of beads per chain N, bead diameter D, chain volume V_{chain}, and angle potential coefficient k_{angle}. The reference homopolymer melt (D = 1d, $k_{angle} = 0k_BT$) is highlighted with a gray background.*

N	D (d)	V_{chain} (d^3)	k_{angle} (k_BT)	β/β_{ref}
232	0.6	26.24	0	1.41
98	0.8	26.27	0	1.09
50	1	26.18	0	1.00
29	1.2	26.24	0	0.90
18	1.4	25.86	0	0.81
12	1.6	25.74	0	0.73
9	1.8	27.48	0	0.65
6	2	25.13	0	0.59
50	1	26.18	2.5	1.54
50	1	26.18	5	2.19
50	1	26.18	7.5	3.51
50	1	26.18	10	4.06
50	1	26.18	12.5	4.76
50	1	26.18	15	5.25
50	1	26.18	17.5	5.35
50	1	26.18	20	5.46

Table S3 *Chain design parameters for semiflexible $A_1B_1A_2B_2A_3$ pentaBCPs, in terms of the bead diameter ratio D_A/D_B, volume fraction of A beads f_A, the fraction of A beads in block A_2 among all A beads in the chain τ_{A_2}, and the total number of beads per chain N, as well as the number of beads in each block.*

D_A/D_B	f_A	τ_{A_2}	N	N_{A_1}	N_{B_1}	N_{A_2}	N_{B_2}	N_{A_3}
1	0.32	0.50	50	4	17	8	17	4
1	0.38	0.50	52	5	16	10	16	5
1	0.46	0.50	52	6	14	12	14	6

Table S4 *Chain design parameters for unequal-bead-diameter (UBD) $A_1B_1A_2B_2A_3$ pentaBCPs, in terms of the bead diameter ratio D_A/D_B, volume fraction of A beads f_A, the fraction of A beads in block A_2 among all A beads in the chain τ_{A_2}, and the total number of beads per chain N, as well as the number of beads in each block.*

D_A/D_B	f_A	τ_{A_2}	N	N_{A_1}	N_{B_1}	N_{A_2}	N_{B_2}	N_{A_3}
0.6	0.36	0.50	50	9	7	18	7	9
0.6	0.39	0.50	48	9	6	18	6	9
0.6	0.42	0.50	52	10	6	20	6	10
0.6	0.46	0.50	50	10	5	20	5	10
0.8	0.34	0.50	48	6	12	12	12	6
0.8	0.37	0.50	52	7	12	14	12	7
0.8	0.40	0.50	50	7	11	14	11	7

0.8	0.44	0.48	51	8	10	15	10	8
1	0.32	0.50	50	4	17	8	17	4
1	0.38	0.50	52	5	16	10	16	5
1	0.46	0.50	52	6	14	12	14	6
1.2	0.35	0.50	50	3	19	6	19	3
1.2	0.42	0.50	54	4	19	8	19	4
1.2	0.45	0.50	50	4	17	8	17	4
1.4	0.34	0.50	50	2	21	4	21	2
1.4	0.37	0.50	46	2	19	4	19	2
1.4	0.42	0.50	58	3	23	6	23	3
1.4	0.44	0.50	54	3	21	6	21	3

RAPSIDY workflow

In our initial round of simulations using our simulated annealing protocol, there were two similar designs, one semiflexible pentaBCP design (f_A = 0.38, *CAR* = 1.4) and one UBD pentaBCP design (f_A = 0.39, *CAR* = 1.4), for which we could not identify an equilibrium morphology as no single morphology formed in a majority of simulation trials. Additionally, we observed an inverted N structure (where the B domains formed the network structure) for two semiflexible pentaBCP designs, f_A = 0.38 and 0.46 with *CAR* = 0.6, which we found at χN = 90, 150, and 200. Our SCFT calculations predicted an analogous phase, the inverted DG, as the equilibrium morphology of a pentaBCP with a similar design (f_A = 0.5 and *CAR* = 0.6 at χN = 40), but we wanted to verify that this newly observed morphology was the actual equilibrium phase and not an artifact of kinetic trapping. We therefore decided to use our RAPSIDY workflow to find the optimal unit cell dimensions of one or more morphologies that were closest to what we observed in the initial trials: we screened DG for the high-*CAR* semiflexible pentaBCP (f_A = 0.38, *CAR* = 1.4), L for the low-*CAR* semiflexible pentaBCPs (f_A = 0.38 and 0.46, *CAR* = 0.6), and both C_6 and DG for the UBD pentaBCP (f_A = 0.39, *CAR* = 1.4).

We base our procedure off the RAPSIDY 1.0 workflow[2] as we do not make use of RAPSIDY 2.0's[3] active learning loop. We screen a set of lattice constants for each phase which defines its unit cell dimensions: the lattice constant is the combined width of A and B domains for L (equivalently, the center-to-center distance between domains of the same type), the cylinder center-to-center distance for C_6, and the side length of the cubic unit cell for DG. We do not attempt to optimize the simulation box shape (i.e., the relative lengths of its dimensions). We screen the following values of the lattice constant: for L, between 8 and 14d in increments of 2d; for C_6, between 8 and 16d in increments of 2d; for DG, between 23 and 32d in increments of 3d. To prevent chain self-interaction we ensure that each dimension of the simulation box is $\geq 30d$, and therefore we find the final simulation box dimensions for the RAPSIDY protocol by replicating (tiling) the unit cell along each axis as needed to meet this criterion. For example, a pentaBCP melt being screened for L with a lattice constant of 8d has a simulation box length of 32d along the L periodic axis and 30d along the non-periodic axes, and we construct a biasing field with 4 complete L unit cells (each with one A and one B lamellar domain).

We begin the RAPSIDY (meta)stability testing protocol for each chosen pentaBCP design, target morphology, and lattice constant by creating a well-mixed melt of pentaBCP chains. We relax the chains initially with only the harmonic bond potential while shrinking to the target box dimensions, after which we enable a soft push-off potential to eliminate bead overlap in preparation for biasing. Then, we switch to a force-capped LJ potential for nonbonded interactions (without changing the harmonic bonded potential) and enable the biasing field corresponding to the morphology unit cell being screened, which we construct analytically for L, C_6 and DG as in our previous work[2]. After biasing is complete, we disable the biasing field and relax the melt with the cut-and-shifted LJ potential for 6×10^6 timesteps ($\Delta t = 0.01\ \tau$) in the NPT ensemble (Nosé–Hoover thermo- and barostat; $T^* = 1$, $P^* = 1$ in reduced LJ units) at the chosen χN. We found it necessary to extend this relaxation period from 10^6 timesteps, as we used in our previous work with RAPSIDY, to 6×10^6 timesteps due to the slower dynamics of some conformationally asymmetric pentaBCPs (particularly semiflexible pentaBCPs). Finally, we evaluate the stability of the biased structure after relaxation by calculating the sum of squared errors (SSE) between the structure factors of the 'just' biased and the fully relaxed melts

$$SSE_{\ln(S(q))} = \sum \left[\ln\left(\frac{q_{i+1}}{q_i}\right) \mathrm{x} \ln\left(\frac{S_2(q_i)}{S_1(q_i)}\right)^2 \right] \quad (1)$$

where $S_1(q_i)$ and $S_2(q_i)$ are the structure factor values at q_i for the just biased and the relaxed melts, respectively. We compute $S(q)$ as the scattering amplitude as in our previous work[4] for 100 log-spaced q vectors with magnitudes between $(2\pi/3d)$ and $(2\pi/30d)$, which correspond to the real-space distances of $3d$ and $30d$, in order to capture information on the melt *mesoscale* structure from $S(q)$.

We find the "optimal" unit cell dimensions of the target morphology as those which showed the least structural change after relaxation, i.e. had the lowest $SSE_{\ln(S(q))}$. Finally, we initialize another melt of the chosen pentaBCP design using the RAPSIDY-optimized simulation box dimensions and then proceed through our simulated annealing protocol (described in the main paper Section 2.3.3). We marked equilibrium morphologies which we identified using this procedure with an asterisk on the semiflexible (main paper's Fig. 5) and UBD (Fig. 6) pentaBCP phase diagrams.

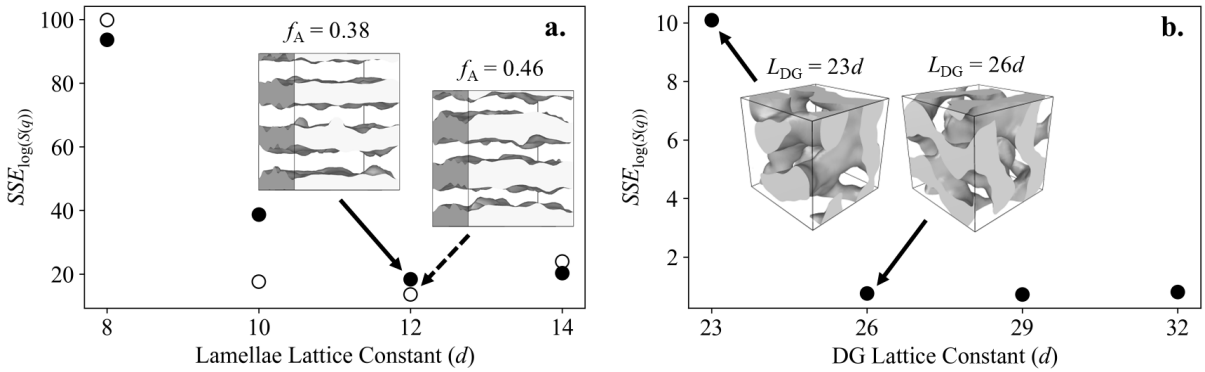

Fig. S1 *RAPSIDY stability profiles for the semiflexible pentaBCPs with (a) $f_A = 0.38$ (filled circles) and 0.46 (empty circles), CAR = 0.6, screened for the L phase and (b) $f_A = 0.38$, CAR = 1.4, screened for the DG phase. The inset images show the A-B isosurfaces of the relaxed configurations of the (a) pentaBCPs with $f_A = 0.38$ (solid arrow) and 0.46 (dashed arrow), CAR = 0.6, screened for L with a lattice constant of 12d, the optimal period for both designs, and (b) the pentaBCP with $f_A = 0.38$, CAR = 1.4 screened for DG with lattice constants of 23d, an unstable DG period, and 26d, the optimal DG period. Note the different y-axis bounds. The isosurfaces are drawn using the method outlined in Section 2.3.5 in the manuscript.*

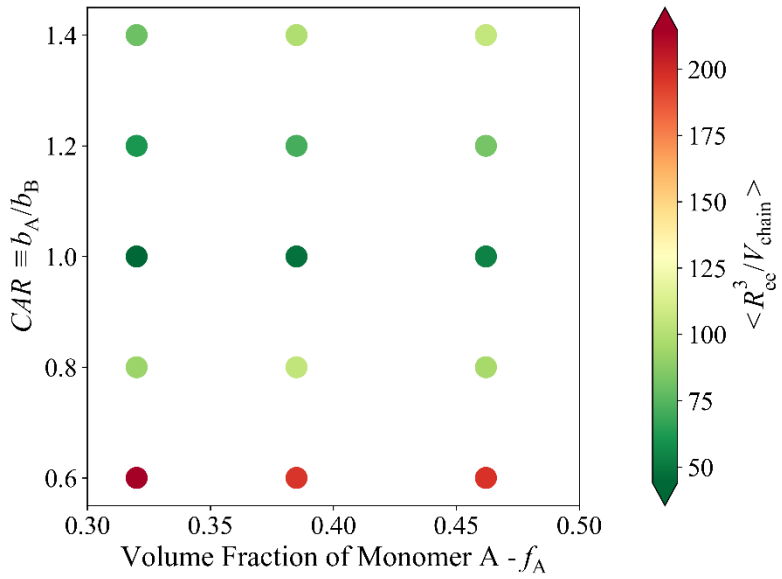

Fig. S2 *The heat map for the chain coordination number representing the average number of interacting chains per pentaBCP chain, quantified as* R_{ee}^3 / V_{chain} *where* R_{ee} *is the chain end-to-end distance and* V_{chain} *is the volume of single pentaBCP chain, defined for semiflexible pentaBCPs as* $V_{chain} = N\left(\frac{4}{3}\pi\left(\frac{1}{2}d\right)^3\right)$. *The pentaBCP designs on the heat map correspond to Fig. 5a in the main manuscript for the phase diagram of semiflexible pentaBCP melts at* $\chi N = 90$. *The* R_{ee} *is sampled from all chains across all three trials, with four sampled frames per each trial in an interval of 5* $\times 10^6$ *timesteps.*

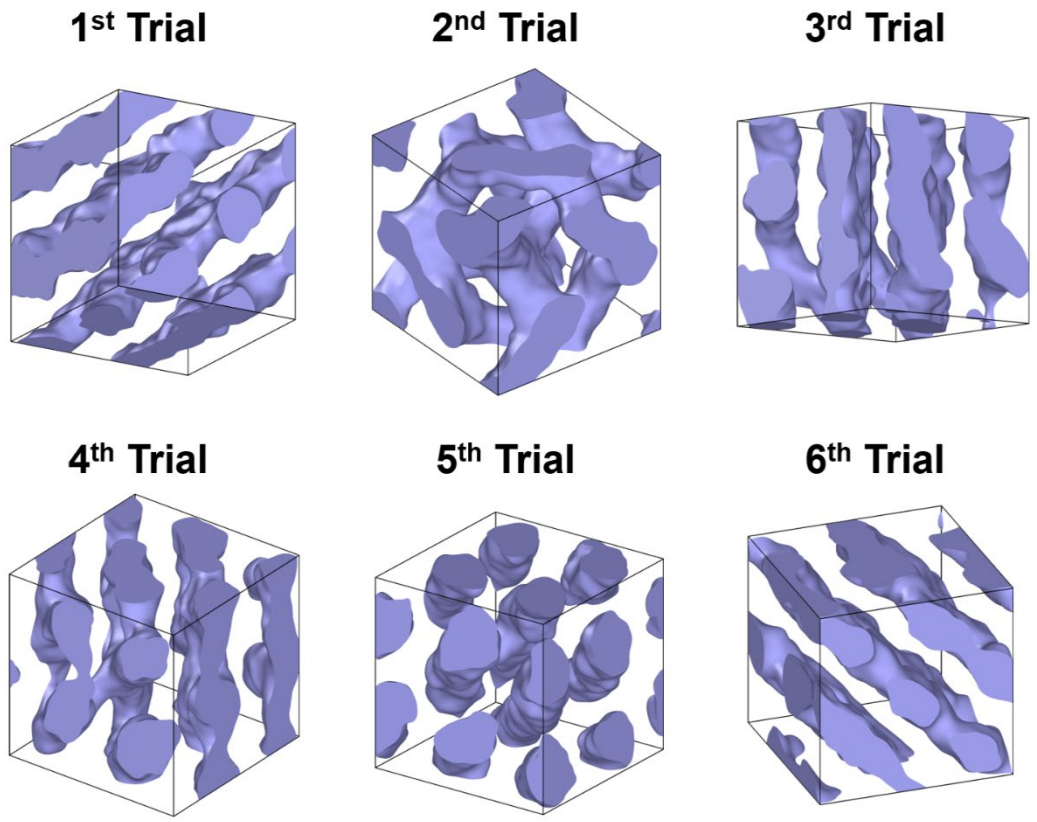

Fig. S3 *The self-assembled morphologies from the six independent trials of MD simulations for the $A_1B_1A_2B_2A_3$ pentaBCP melts at $\chi N = 200$ with the semiflexible chain model (CAR = 1.4 and $f_A = 0.38$). The morphologies represent the A domains defined by the A-B interfaces using the Gaussian density method described in Section 2.3.5 of the main manuscript. The various self-assembled morphologies are observed from the six trials: perforated lamellae (1st and 6th trials), double gyroid (2nd trial), frustrated perforated lamellae or frustrated cylinders (3rd and 4th trials), and hexagonally-packed cylinders (5th trial), which motivated us to utilize RAPSIDY workflow described above to find the optimal simulation box size for the equilibrium double gyroid (DG) phase.*

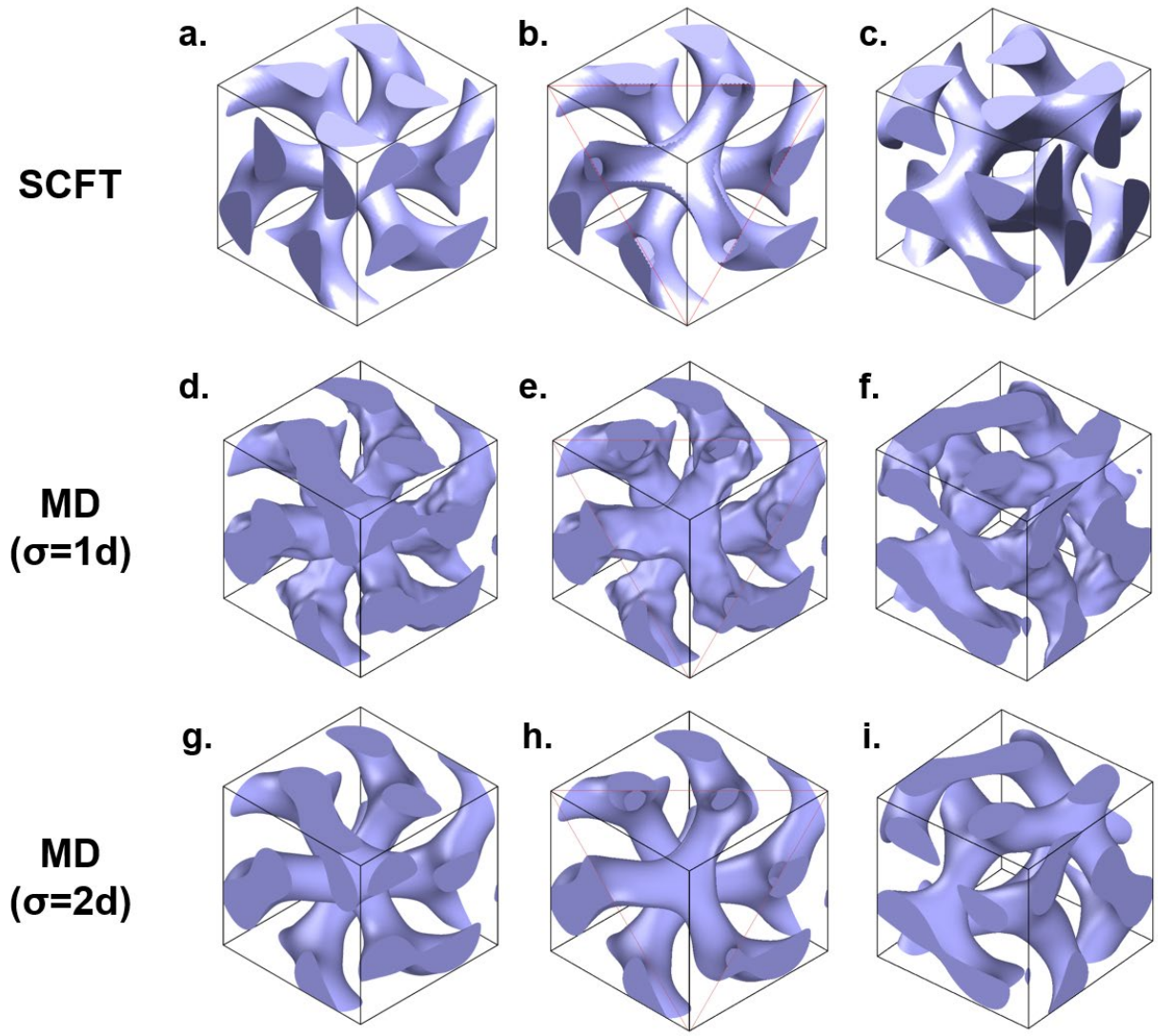

Fig. S4 *The comparison of the DG morphology between SCFT calculations and MD simulations. (a-c) The representative DG morphologies from the SCFT calculations which have perfect $Ia\bar{3}d$ space group symmetry. (d-i) The DG morphologies observed in the MD simulations for the $A_1B_1A_2B_2A_3$ pentaBCP melts at $\chi N = 200$ with the semiflexible chain model (CAR = 1.4 and f_A = 0.38), where the RAPSIDY-informed simulation box size is used. The DG morphologies for the MD simulations represent the A domains defined by the A-B interfaces using the Gaussian density method with standard deviations σ for the Gaussian function of (d-f) 1d and (g-i) 2d. For the comparison of the DG unit cell between SCFT and MD simulation, the positions of beads in the MD simulations, which are used to construct the A-B interfaces, are translated along the z axis accounting for the periodic boundary condition. The first column (a,d,g) compares the views along*

the [1 1 1] direction of the DG unit cell, the second column (b,e,h) compares the same view but with sliced plane (denoted by the red triangles) to reveal the three-fold connectors of DG morphology, and the third column (c,f,i) compares a different angle view to present the two interwoven networks with opposite chirality in the DG morphology.

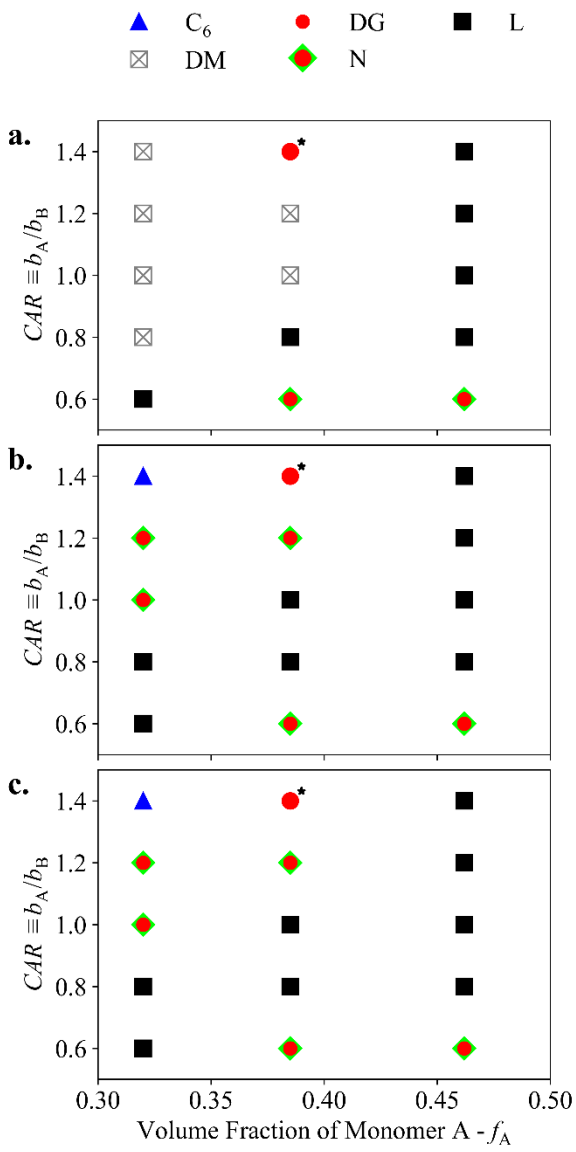

Fig. S5 *(a,b) The same phase diagrams shown in Fig. 5 in the main manuscript for $A_1B_1A_2B_2A_3$ pentaBCPs at (a) $\chi N = 90$ and (b) $\chi N = 150$ from the MD simulations of semiflexible chain models. (c) The phase diagram at $\chi N = 200$.*

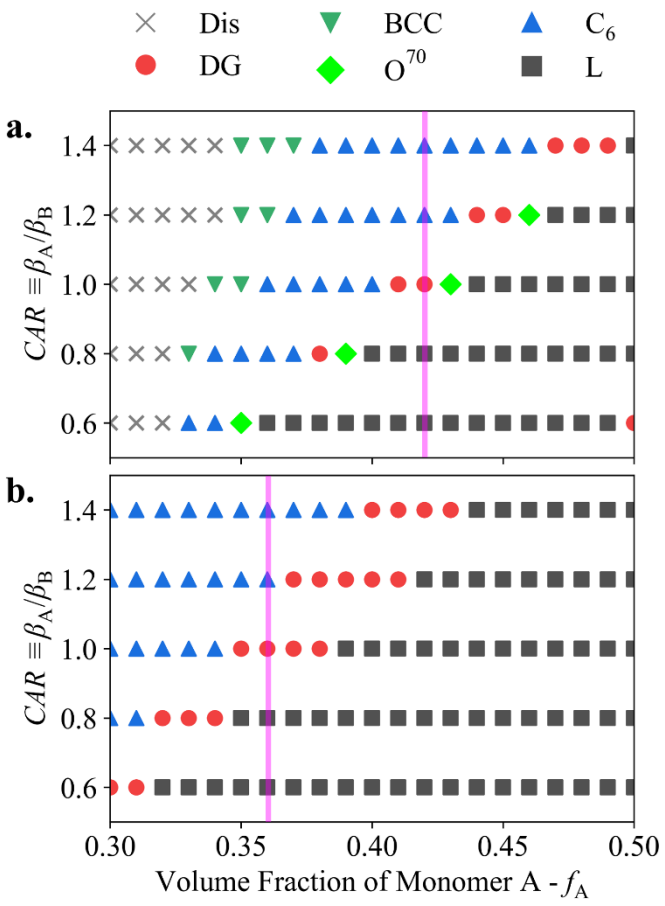

Fig. S6 *The same SCFT phase diagrams shown in Fig. 4 in the main manuscript for $A_1B_1A_2B_2A_3$ pentaBCPs at (a) $\chi N = 40$ and (b) $\chi N = 60$ with vertical lines ($f_A = 0.42$ and $f_A=0.36$) overlaid to highlight the ordered phase sequence L → DG (Network) → C_6 as CAR increases.*

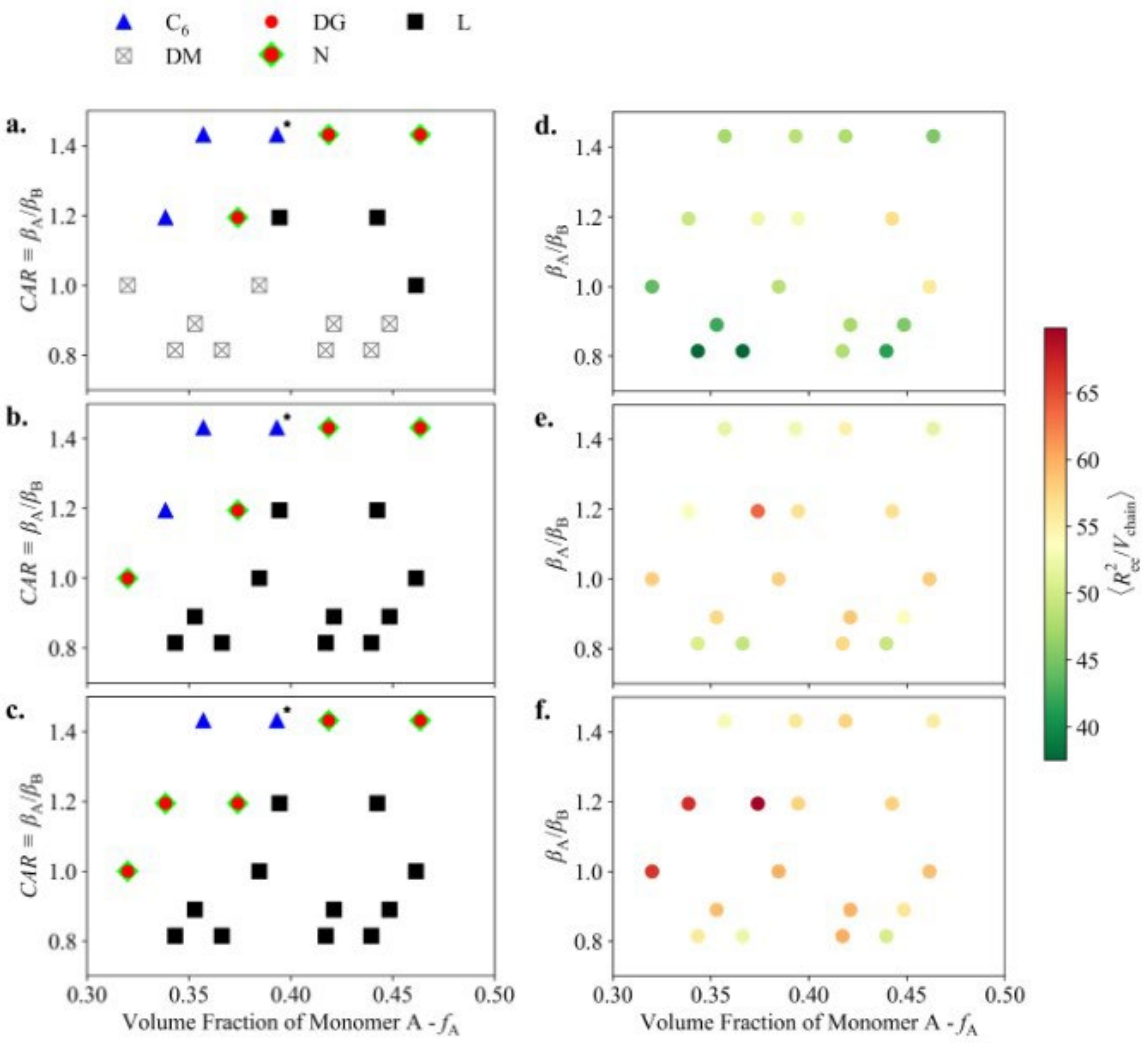

Fig. S7 *Equilibrium morphologies and average number of interacting chains per single pentaBCP chain (R_{ee}^3/V_{chain}) of UBD pentaBCPs of varying f_A and CAR, sampled as in Fig. S2 from MD simulation at (a,d) $\chi N = 90$, (b,e) $\chi N = 150$, and (c,f) $\chi N = 200$.*

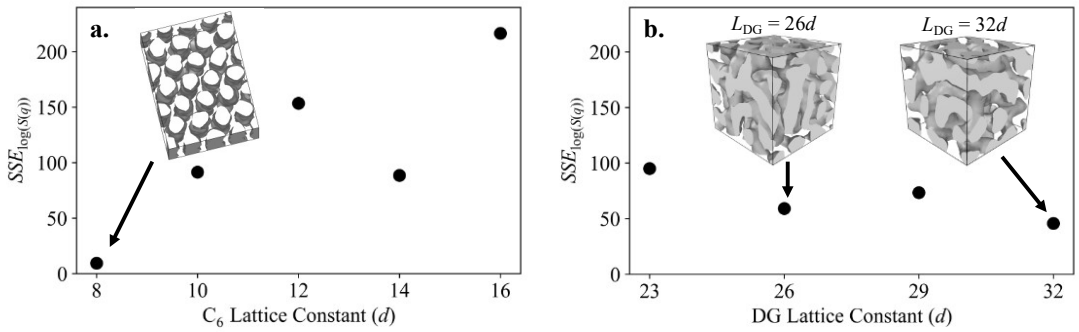

Fig. S8 *RAPSIDY stability profiles for the UBD pentaBCP with f_A = 0.39, CAR = 1.4, screened for the (a) C_6 and (b) DG phases. The inset images show the A-B isosurfaces of the relaxed configurations of the melts biased into (a) C_6, with a lattice constant of 8d, and (b) DG with lattice constants of 26d, the optimal DG lattice constant for the analogous semiflexible pentaBCP (as shown in Fig. S1b), and 32d, the optimal DG lattice constant for this UBD pentaBCP design. The isosurfaces are drawn using the method outlined in Section 2.3.5 in the manuscript.*

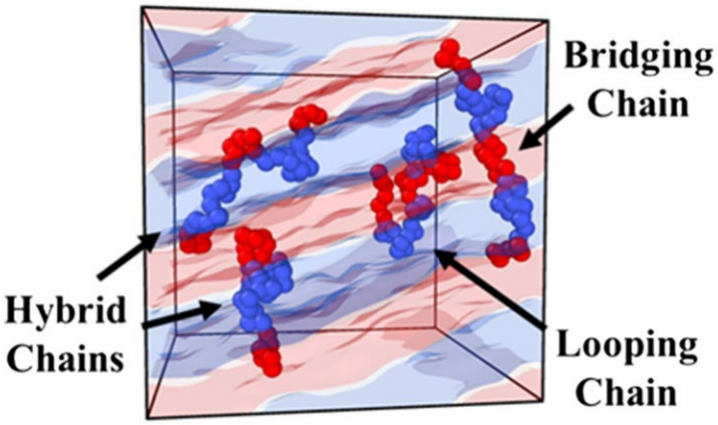

Fig. S9 *Schematic of $A_1B_1A_2B_2A_3$ pentaBCPs depicting the looping, hybrid, and bridging chain configurations, which are attributed to the low, medium, and high R_{ee} peaks (modes), respectively, in the histograms of ordered morphologies shown in ESI† Fig. S10a-d and ESI† Fig. S11a,b, and d. The schematic is reprinted from our previous paper on pentaBCP melt phase behavior.*[4]

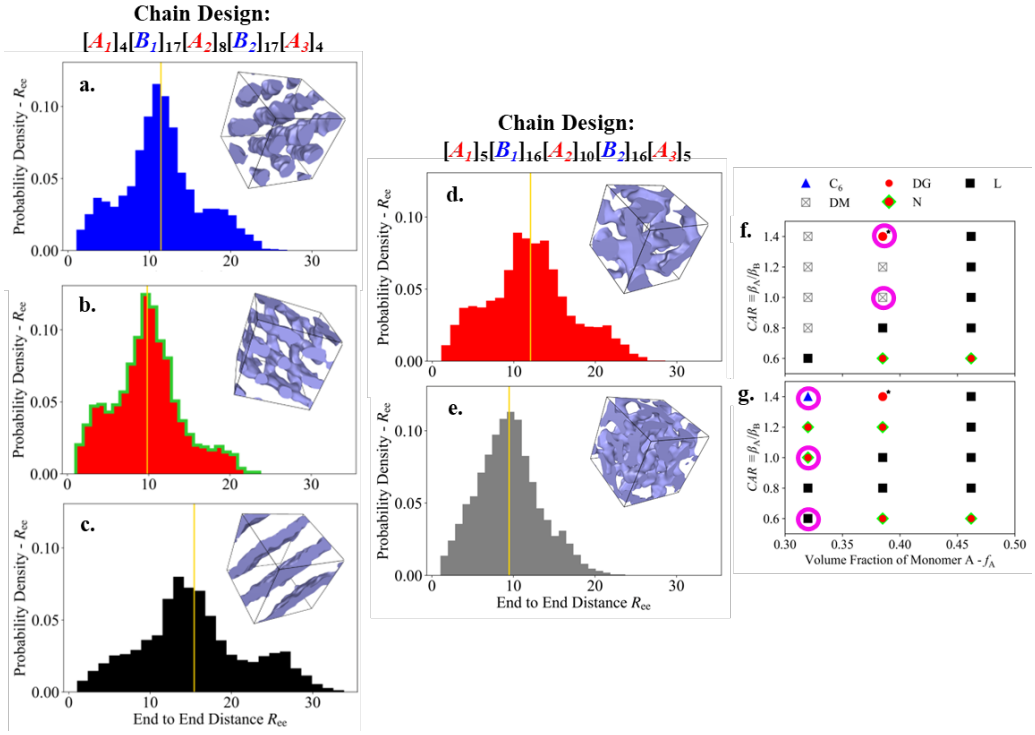

Fig. S10 *Distributions of chain end-to-end distance R_{ee} in each morphology ((a) C_6, (b) N, (c) L, (d) DG, and (e) DM shown in insets) observed in MD simulation of the semiflexible chain model for the chain designs highlighted with magenta circles in the (f) $\chi N = 90$ and (g) $\chi N = 150$ phase diagrams. Both phase diagrams are identical to those presented in Fig. 5 in the main manuscript. The chain design parameters for the first column (a) $f_A = 0.32$, CAR = 1.4, (b) $f_A = 0.32$, CAR = 1.0, (c) $f_A = 0.32$, CAR = 0.6, and those for the second column are (d) $f_A = 0.38$, CAR =1.4 and (e) $f_A = 0.38$, CAR = 1.0. The full chain designs on given on top of either column, where the subscripts outside the brackets denote the degree of polymerization of that block of the $A_1B_1A_2B_2A_3$ pentaBCPs. The insets of the histograms present the A domain morphologies identified by the isosurfaces where the A bead density is 50% of bulk bead density. The R_{ee} is sampled from all chains across the two trials that form the majority morphologies, including four sampled frames per trial in an interval of 5×10^6 timesteps. The average chain end-to-end distance R_{ee} for each histogram is denoted by the gold vertical lines and is given in the text below.*

To analyze the chain conformations of the $A_1B_1A_2B_2A_3$ pentaBCPs and how they are affected by the self-assembled morphology and the chain designs, in ESI† Fig. S10, we plot the histograms of chain end-to-end distance R_{ee} in each morphology observed in the MD simulations with the 'semiflexible chain model', For comparison, we select five different chain designs that exhibit each morphology we observed for semiflexible pentaBCPs (C_6, N, L, DG, and DM in ESI† Fig. S10a-e). The histograms show that all the ordered phases exhibit three modes, while the DM phase exhibits a monomodal distribution. The three modes are explained by the three different types of chain conformations the $A_1B_1A_2B_2A_3$ pentaBCPs adopt during self-assembly into ordered morphologies. The three different types of chain conformations, classified as looping, hybrid, and bridging chain conformations, were discussed and quantified in our previous paper[4] for conformationally symmetric $A_1B_1A_2B_2A_3$ pentaBCPs. Specifically, the low, medium and high R_{ee} values evident in the histograms of ordered morphologies (ESI† Fig. S10) correspond to the looping, hybrid, and bridging chain conformations as depicted in ESI† Fig. S9. These three modes in the R_{ee} distribution for the pentaBCPs are considered a unique feature not observed from the simpler BCPs like diBCPs, due to the multiple combinations of looping and bridging configurations of each constituent block that are possible in the pentaBCPs.

Among the ordered phases at $f_A = 0.32$ and $\chi N = 150$ but with different *CAR* (ESI† Fig. S10a-c), the $\langle R_{ee} \rangle$ averaged over the all pentaBCP chains is highest for *CAR* = 0.6 (ESI† Fig. S10c, $\langle R_{ee} \rangle = 15.43d$), medium for *CAR* = 1.4 (ESI† Fig. S10a, $\langle R_{ee} \rangle = 11.42d$), and lowest for *CAR* = 1.0 (ESI† Fig. S10b, $\langle R_{ee} \rangle = 9.82d$). The results indicate that the conformationally symmetric pentaBCP chains (*CAR* = 1.0), where both A and B type blocks are flexible, have the lowest $\langle R_{ee} \rangle$, while conformationally asymmetric pentaBCPs, where one of A or B type blocks are semiflexible, are more likely to adopt extended chain conformations and have higher $\langle R_{ee} \rangle$ values. Especially when the majority blocks (B type block) are stiffer than the minority blocks (A type blocks), the population of bridging chain conformations becomes appreciable as shown in ESI† Fig. S10c with the large R_{ee} peak, giving rise to much higher $\langle R_{ee} \rangle$ as compared to when minority blocks are stiffer than the majority blocks (ESI† Fig. S10a).

The R_{ee} distributions in the second column of ESI† Fig. S10, for semiflexible pentaBCPs with $f_A = 0.38$ and $\chi N = 90$, demonstrate the different chain conformations adopted in ordered (DG, ESI† Fig. S10d) and disordered (DM, ESI† Fig. S10e) morphologies. Chains of the same design adopt one of several categories of chain conformation in the high-*CAR* DG phase, leading to a

higher average R_{ee}, while their conformations are more homogenous and shorter on average for the DM phase at $CAR = 1$.

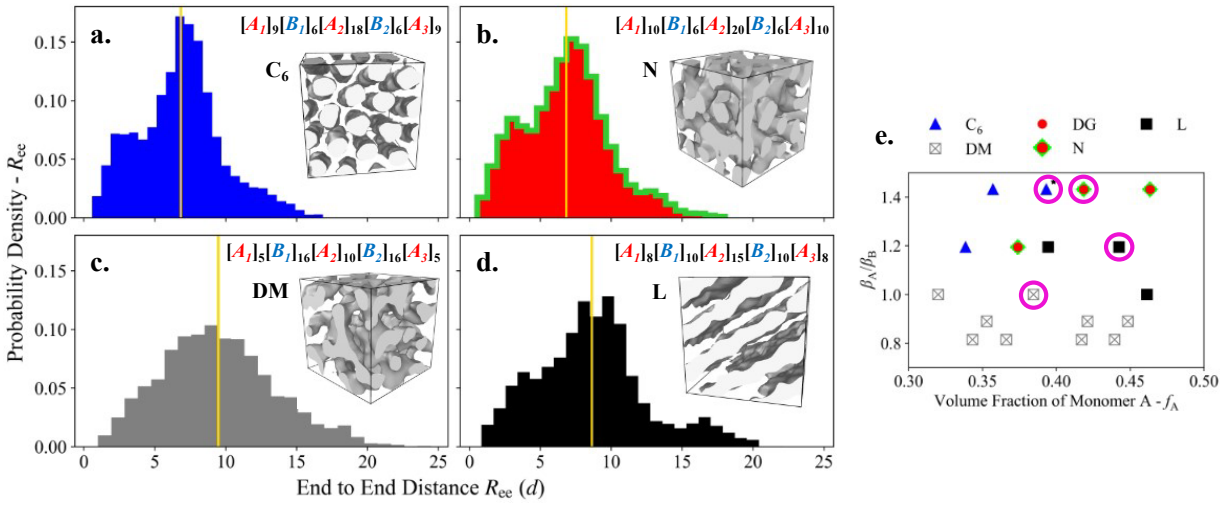

Fig. S11 *Distributions of chain end-to-end distance R_{ee} from simulated melts of unequal-bead-diameter $A_1B_1A_2B_2A_3$ pentaBCPs in the (a) hexagonally-packed cylinders (C_6), (b) network (N), (c) disordered microphase (DM), and (d) lamellae (L) morphologies, along with the (e) UBD pentaBCP phase diagram at $\chi N = 90$ (Fig. 6a) on which the sampled designs are marked with magenta circles. The chain conformations are sampled as those in ESI† Fig. S10. The inset of each distribution includes the full chain design, an isosurface drawn on the A-B interface, and a label for the morphology. The average R_{ee} of each distribution is marked with a gold vertical line and is noted in the text below.*

We display R_{ee} distributions sampled from UBD pentaBCPs in ESI† Fig. S11. A similar distinction in chain conformations for the DM phase vs ordered phases is observed for the UBD pentaBCPs as with the semiflexible pentaBCPs. The R_{ee} distribution sampled from the DM phase (ESI† Fig. S11c) is monomodal, indicating the lack of categorically different chain conformations, where the distributions for the ordered phases (ESI† Fig. S11a, b, and d) have at least two distinct peaks. The average R_{ee} for each population, denoted with the gold line on each distribution, are as follows: $\langle R_{ee} \rangle_{C_6} = 6.84$d, $\langle R_{ee} \rangle_{N} = 6.83$d, $\langle R_{ee} \rangle_{DM} = 9.48$d, and $\langle R_{ee} \rangle_{L} = 8.63$d. As demonstrated in

Fig. 7c of the main text, the variation in average R_{ee} for UBD pentaBCPs can mostly be attributed to differences in contour length L_c resulting from changing A bead diameter D_A while maintaining a constant number of beads per chain N.

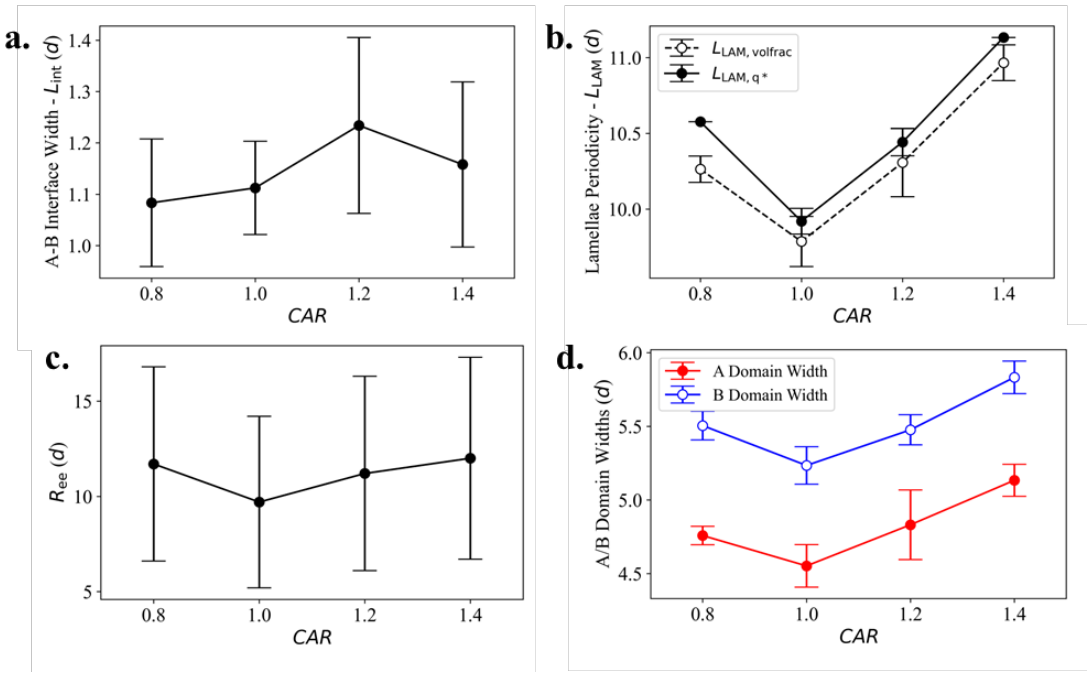

Fig. S12 *(a) A-B interface width, (b) lamellae periodicity L_{LAM}, (c) chain end-to-end distance R_{ee}, and (d) A and B domain widths for the four semiflexible pentaBCPs analyzed in Fig. 7 of the main text. L_{LAM} is quantified using the profiles of A (filled red circles) and B (empty blue circles) bead volume fraction along the lamellae normal axis, $L_{LAM,volfrac}$, as well as the real-space length corresponding to the q* peak of the melt's structure factor, $L_{LAM,q^*} = 2\pi/q^*$. All quantities are sampled as described in Section 2.3.6 of the main manuscript.*

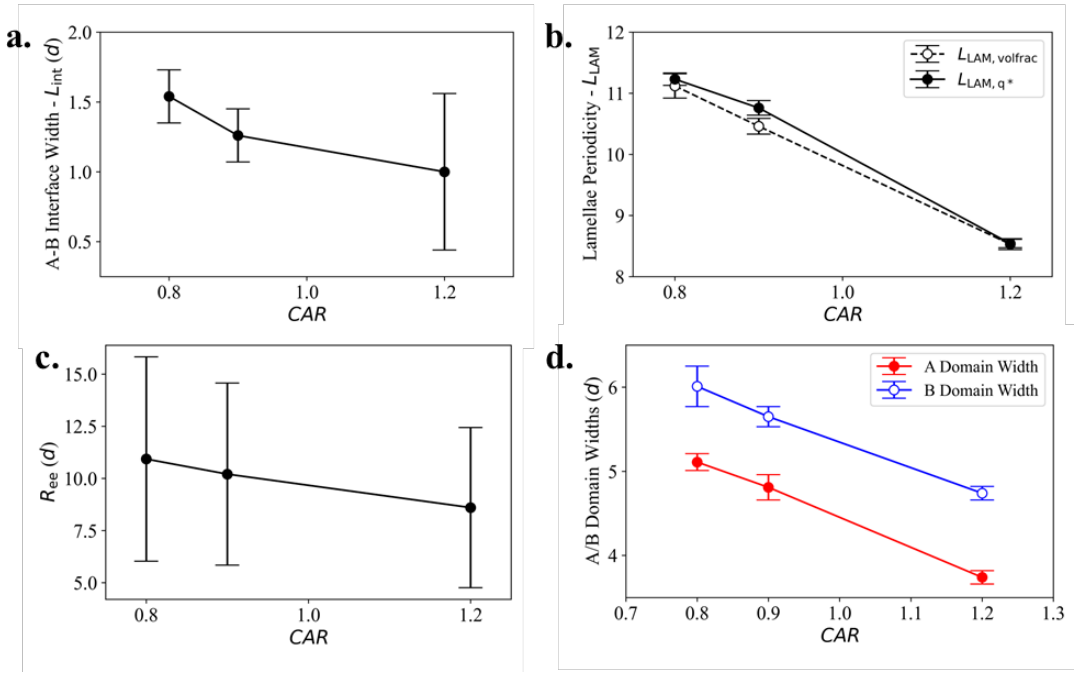

Fig. S13 *(a) A-B interface width, (b) lamellae periodicity L_{LAM}, (c) chain end-to-end distance R_{ee}, and (d) A and B domain widths for the three UBD pentaBCPs analyzed in Fig. 7 of the main text. L_{LAM} is quantified using the profiles of A (filled red circles) and B (empty blue circles) bead volume fraction along the lamellae normal axis, $L_{LAM,volfrac}$, as well as the real-space length corresponding to the q* peak of the melt's structure factor, $L_{LAM,q*} = 2\pi/q*$.*

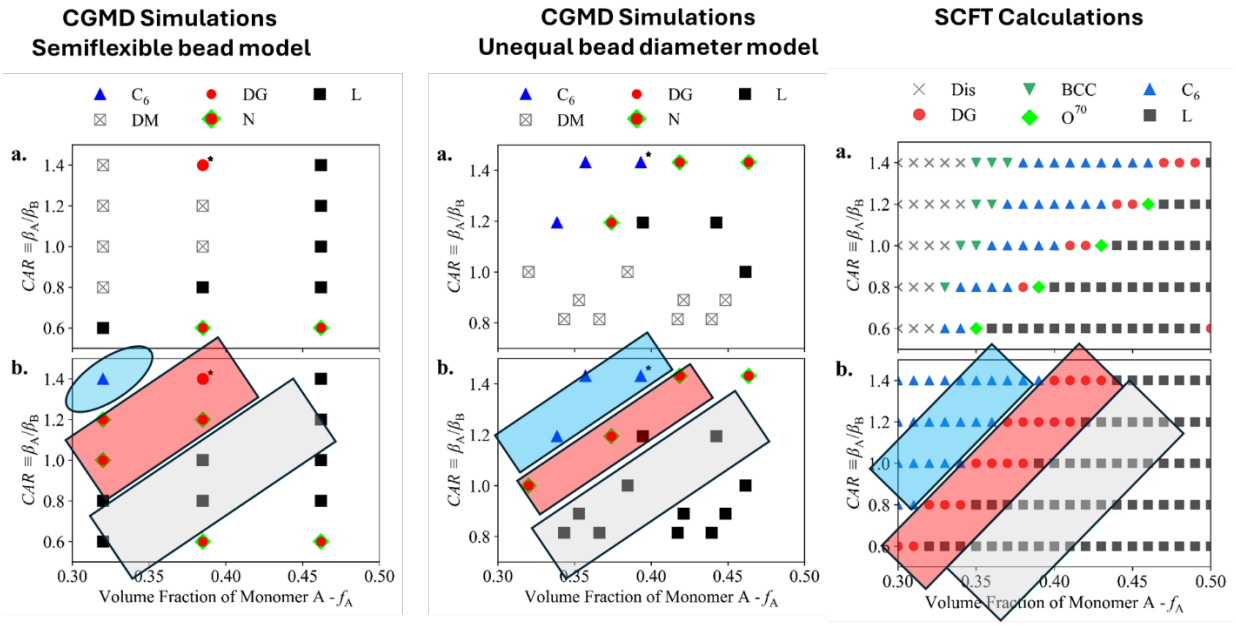

Fig. S14 *Copy of Fig. 5, Fig. 6, and Fig.4 of main manuscript to see qualitative similarities in the phase diagrams in the lower panels of these figures representing χN = 150 for Fig. 5 and Fig. 6, and χN = 60 for Fig. 4.*

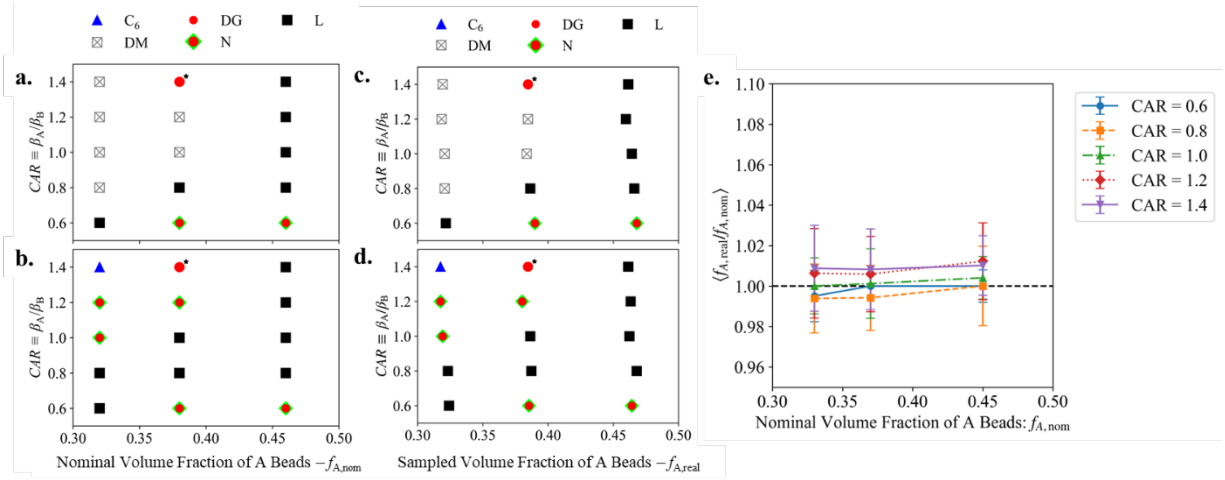

Fig. S15 *Phase diagrams for semiflexible pentaBCPs at (a,c) χN = 90 and (b,d) χN = 150. Equilibrium morphologies are plotted against (a,b) $f_{A,nom}$ and (c,d) $f_{A,real}$. (e) Average $f_{A,real}/f_{A,nom}$ plotted against $f_{A,nom}$ for semiflexible pentaBCPs with CAR = 0.8, 0.9, 1.0, 1.2, and 1.4. The black*

dashed horizontal line is $f_{A,real}/f_{A,nom}$ = 1. Error bars represent ± 1 standard deviation in the sampled quantity.

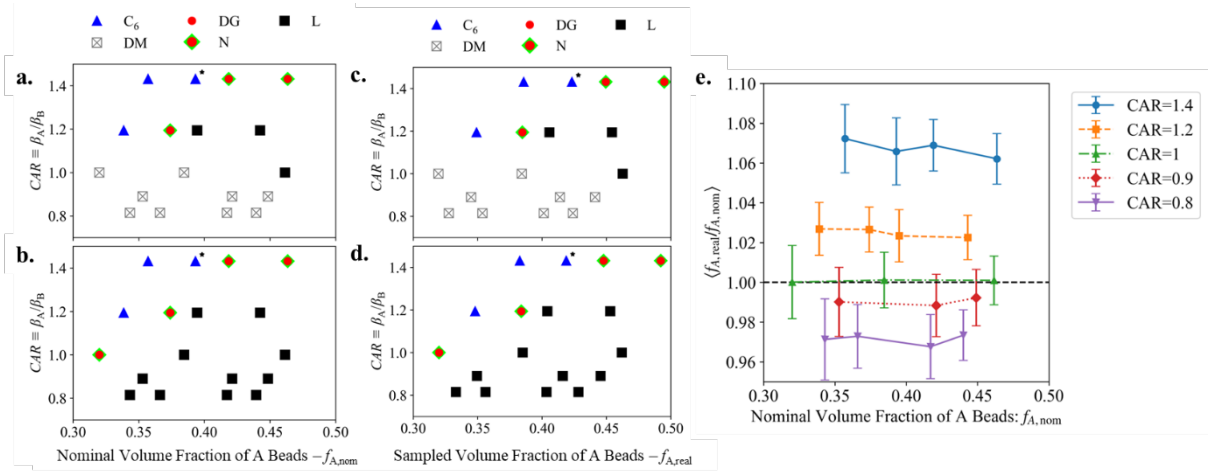

Fig. S16 *Phase diagrams for UBD pentaBCPs at (a,c) χN = 90 and (b,d) χN = 150. Equilibrium morphologies are plotted against (a,b) $f_{A,nom}$ and (c,d) $f_{A,real}$. (e) Average $f_{A,real}/f_{A,nom}$ plotted against $f_{A,nom}$ for UBD pentaBCPs with CAR = 0.8, 0.9, 1.0, 1.2, and 1.4. The black dashed horizontal line is $f_{A,real}/f_{A,nom}$ = 1. Error bars represent ± 1 standard deviation in the sampled quantity.*

To sample the partial molar bead volume as a function of chain composition and *CAR*, we calculated the radial distribution function (RDF, $g(r)$) between beads of the same type and used the radial distance of the first peak as the corresponding bead diameter; i.e., D_A is sampled from $g_{AA}(r)$ and D_B from $g_{BB}(r)$. We then use these sampled D_A and D_B to calculate $f_{A,real}$ and designate the f_A calculated by assuming $D = \sigma$ as $f_{A,nom}$, and compare phase diagrams for semiflexible and UBD pentaBCPs using either f_A in Fig. S15 and Fig. S16. We also present the ratio $f_{A,real}/f_{A,nom}$ for different compositions and *CAR* in Fig. S15e and Fig. S16e.

References

1. A. Arora, J. Qin, D. C. Morse, K. T. Delaney, G. H. Fredrickson, F. S. Bates and K. D. Dorfman, *Macromolecules*, 2016, **49**, 4675-4690.
2. V. Liao, T. Myers and A. Jayaraman, *Soft Matter*, 2024, **20**, 8246-8259.
3. V. Liao and A. Jayaraman, *JACS Au*, 2025, **5**, 2810-2824.
4. S. J. Park, T. Myers, V. Liao and A. Jayaraman, *Mol Syst Des Eng*, 2024, **9**, 1235-1253.